

Asymmetric self-organization accompanying a thermoinduced spin transition with symmetry breaking: Microscopic modeling

Ahmed Slimani ^{1,2,*} and Kamel Boukheddaden^{3,†}

¹*Sciences and Engineering department, Sorbonne University Abu Dhabi, Al Reem island, Abu Dhabi, PO Box 38044, United Arab Emirates*

²*Laboratoire des Matériaux Multifonctionnels et Applications, Département de physique, Faculté des Sciences de Sfax, University of Sfax, Route de Soukra km 3.5, B.P. no. 1171, 3000, Sfax, Tunisia*

³*Groupe d'Etudes de la Matière Condensée, CNRS-Université de Versailles, 45, Avenue des Etats Unis, F-78035 Versailles Cedex, France*



(Received 23 February 2023; revised 3 June 2023; accepted 27 July 2023; published 28 August 2023)

A microscopic elastic model allowing a symmetry breaking upon a spin transition is developed based on competing interactions between the nearest and next-nearest neighbors. The model yields a structurally degenerated high-spin state with a diamond-shaped cell and a nondegenerated low-spin state with a square-shaped cell. We investigated the effect of the symmetry change of the unit cell on the thermoinduced spin transition by monitoring the ratio of the elastic energies involved in the nearest and next-nearest neighbors. The simulations are performed on a deformable two-dimensional lattice made of spins $S = \pm 1$ (representing the high-spin and low-spin molecules) coupled with springs. The numerical resolution of the model is based on the Monte Carlo metropolis approach, running on spins and positions variables. The simulations of the thermoinduced spin transition disclose asymmetric thermal hysteresis loops with quite different domain distributions on the heating and cooling branches. The analysis of the magnetic and structural properties pointed out that the spin transition with symmetry breaking is dependent on the sign of the thermal gradient. We demonstrated that the nucleation and growth process of spin domains might contrast with the structural self-organization of the lattice according to the energetic contribution of the symmetry breaking. Indeed, the examination of the spatial organization aspects revealed that the structural and elastic anisotropy in the lattice hinders the long-range character of the intermolecular interactions. The lattice configurations show a labyrinthlike structure during a transition from high-symmetry to low-symmetry phases and a multidomain structure upon a transition in the other way around regardless of the spin state in both phases. Furthermore, we found that thermal fluctuations have a crucial role depending on the thermal gradient and on the direction of evolution of the symmetry (reducing or increasing). We demonstrated that stepped and even incomplete spin transitions could be obtained by adjusting the elastic contribution responsible for the symmetry breaking.

DOI: [10.1103/PhysRevB.108.064107](https://doi.org/10.1103/PhysRevB.108.064107)

I. INTRODUCTION

The spin crossover (SCO) phenomenon is observed in complexes with transition metal, belonging to the d^4 - d^7 electronic configuration. Such systems exhibit magnetic bistability between the high-spin (HS) and low-spin (LS) states [1]. The spin switching might be triggered by several stimuli as temperature, pressure, light, magnetic, and electric fields [2–10]. For example, under the effect of the ligand field, the d orbitals of Fe(II) are split into e_g and t_{2g} orbitals when subjected to an octahedral symmetry. The LS state is a singlet (with a total spin quantum number $S = 0$), while the HS state is a quintet (with a total spin quantum number $S = 2$). The bistability of spin crossover compounds is very promising to integrate emerging technological applications as high-density information storage, display devices, and microsensors [11–13]. Indeed, in spin crossover materials the structural and magnetic properties are strongly correlated, to such an extent that the spin switching of the metal ion induces

structural rearrangements at the molecular level and are reflected at the macroscopic scale on several physical properties: magnetism, optical absorption, volume, shape of the crystal, rigidity, etc. [14–21].

The structural resolution of spin crossover crystals demonstrated the presence of microstructures with structurally self-organized lattices and phases coexistence [22–35]. Moreover, the spin crossover phenomenon may also involve symmetry breaking alongside intermolecular rearrangements [23,30,36–43]. Prior reports have revealed interesting evolutions of the high-spin fractions during the spin transition, in relation with the change in the space groups of the studied materials in some Fe(II) based SCO solids, which were attributed to the crystallographic symmetry breaking. Indeed, the latter mechanism is behind the appearance of nonlinear response as in tetrathiafulvalene-pchloranil (TTF-CA) [44], a charge-transfer molecular crystal. The latter undergoes a phase transition with a symmetry breaking, where intra- and intermolecular rearrangements along changes at the electronic states were observed. When the TTF-CA is excited in the region of the charge-transfer band (i.e., from 0.6 to 1.55 eV) a threshold excitation density is needed in order to start the phototransformation. Such an observation, characteristic of

*ahmed.slimani@sorbonne.ae

†kamel.boukheddaden@uvsq.fr

a highly nonlinear process, clearly indicates that a single charge-transfer excitation cannot generate a macroscopic domain [44]. That is why studying symmetry breaking is a crucial step required to understand the underlying mechanisms behind the appearance of microstructures in spin crossover systems [34–39]. For example, in $[Fe(2-pic)_3]Cl_2EtOH$ ($pic = picolylamine$), a thermally induced two-step SCO behavior, in which alternating HS zigzag chains and a disordered mixture of HS and LS molecules was observed in the plateau region [42]. Furthermore, its propanol analog revealed quite an interesting chessboardlike pattern of HS and LS molecules at the value of the HS fraction, $n_{HS} \approx 0.5$ [45]. Another interesting SCO compound of formula $Fe[HC(3, 5 - Me_2pz)_3](BF_4)_2$ [with $HC(3, 5 - Me_2pz)_3 = scorpionatelike$ tridentate ligand $tris(3, 5 - dimethyl - 1 - pyrazolyl)methane$] exhibited an intermediate phase, where the molecules of the same spin state are organized in alternated layers [46]. Most of these samples involve a crystallographic symmetry breaking as in the complex $Fe[H_2B(pz)_2]_2(phen)([H_2B(pz)_2]_2 = dihydrobis(pyrazolyl)borate; phen = 1, 10-phenanthroline)$ [47]. The latter system exhibited a complete one-step spin transition between monoclinic (HS) and triclinic (LS) phases, contrasting with the previous examples, showing intermediate phases associated with half-step and/or two-step transitions.

Thanks to the cooperative character of spin crossover systems, the structural changes, induced by the spin transition, deploy through elastic interactions or lattice acoustic phonons, and thus manifest themselves at the macroscopic level [48–53]. Indeed, the nature of the bonds (π - π interactions, van der Waals, hydrogen bonding, etc.) is a crucial parameter, since the molecular changes are cooperatively conveyed towards the neighboring sites through the intermolecular interactions. Several theoretical models explained the spin transition based on the synergy between long-range and short-range elastic interactions [29,32,33,54–66]. To date, although the symmetry breaking has been well described from the experimental point of view, the physical mechanisms behind the short- and long-range ordering over the lattice always raise curiosity. Some recent theoretical works investigated the intrinsic elastic frustration in the lattice and led to a rich variety of complex self-organizations of spin domains attributed to the symmetry breaking [61–64,67–70]. The present contribution aims to investigate the effect of symmetry breaking as well as the synergy between short-range and long-range interactions on the spin transition. The paper is organized as follows. Section II presents the theoretical details. Section III discusses the effects of symmetry breaking on the thermoinduced spin transition, the impact of the competition of interactions between the nearest and next-nearest neighbors on the transition, as well as the role of the thermal gradient in the spatiotemporal aspects. Our conclusions are drawn in the final section.

II. MODEL

We consider a two-dimensional (2D) lattice of 50×20 molecules with a parallelogram fixed topology and open boundary conditions. The atoms can move only inside the plane. Each node has four nearest neighbors (NN) and four

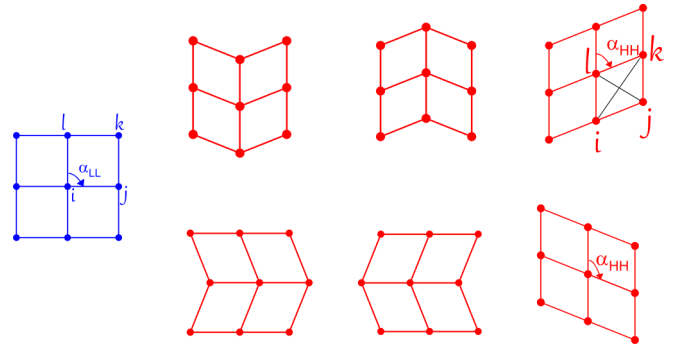


FIG. 1. Lattice schemes showing the symmetry difference between the LS (blue lattice) and HS (red lattices) states. j, l stand for the nearest neighbors of site i and the next nearest neighbors are designated by k . In the LS state $\alpha_{LL} = 90^\circ$, while in the HS state $\alpha_{HH} = 70^\circ$.

next-nearest neighbors (NNN). For each node, indexed i , a fictitious spin, S_i , is associated. The spin may have two states, HS and LS, described by their respective eigenvalues $+1$ and -1 . The interactions between NN and NNN spins take place through springs. In this model, the equilibrium distance between two nodes depends on the values of the connected spin states. The Hamiltonian is written so as to break the symmetry of the lattice when switching from the LS to HS state, via a quartic potential that controls the bond lengths of NNN. In the LS state, the cells of the lattice are perfectly square shaped, unlike the HS state, where each cell may be stretched along one of its diagonals to form a diamond shape (see the schematic view of Fig. 1). We have to mention that this symmetry breaking was analyzed in a prior work [70]. In the latter, the NNN interaction was written in the form of a quartic potential that controls the diagonal difference in each cell of the lattice. However, we discovered recently that, in the case of very strong NNN interactions compared to those of NN, this NNN potential may generate an overlapping of the unit cells in the HS state. The latter configuration verifies the equilibrium of the quartic potential but it is unphysical. Nevertheless, such an overlapping is a rare event because it requires a huge displacement of the neighboring sites which is extremely costly in energy. That is why we propose here a new Hamiltonian that includes a stable form for the NNN potential and whose expression is given below:

$$H = \sum_i \frac{(\Delta - k_B T \ln g) S_i}{2} + \sum_{i,j} A [r_{ij} - R_0(S_i, S_j)]^2 + \sum_{i,k} B [d_{ik} - d_0^+(S_i, S_k)]^2 [d_{ik} - d_0^-(S_i, S_k)]^2. \quad (1)$$

In Eq. (1), Δ is the ligand-field energy and $-k_B T \ln g$ is the entropic contribution (electronic, orbital, and vibrational) arising from the degeneracy g ratio of the spin states, which favors the HS ($S = +1$) state at high-temperature due to its large electrovibrational degeneracy. In Hamiltonian (1), the second (respectively third) term represents the energy of elastic interactions, E_{NN} (respectively E_{NNN}), between NN (respectively NNN) sites, with corresponding equilibrium bond length $R_0(S_i, S_j)$ (respectively $d_0^\pm(S_i, S_k)$) linking the nodes i

and j (respectively i and k), the values of which depend on the connected spin states. Thus, for the nearest neighbors, we take $R_0(+1, +1) = R_0^{\text{HH}}$, $R_0(+1, -1) = R_0(-1, +1) = R_0^{\text{HL}}$, and $R_0(-1, -1) = R_0^{\text{LL}}$, where R_0^{HH} and R_0^{LL} are the respective equilibrium distances between HS-HS and LS-LS sites. The equilibrium distance R_0^{HL} between NN HS and LS sites is fixed for simplicity as $R_0^{\text{HL}} = \frac{R_0^{\text{HH}} + R_0^{\text{LL}}}{2}$. It is then straightforward to demonstrate that the expression of R_0 with respect to the spin states writes

$$R_0(S_i, S_j) = R_0^{\text{HL}} + \frac{\delta R}{4}(S_i + S_j), \quad (2)$$

where $\delta R = R_0^{\text{HH}} - R_0^{\text{LL}}$ is the lattice misfit between the HS and the LS phases.

Now, to define the equilibrium bond lengths for the NNN, we consider the change of symmetry of the unit cells in the HS state (illustrated in Fig. 1), where the lattice has two possible orientations, according to the directions of the short and long diagonals of the unit cell, unlike the single solution of the squared unit cell in the LS state. Simple geometric calculations give the expressions of $d_0^\pm(S_i, S_k)$, the two equilibrium NNN diagonal distances, in terms of the NN distance, R_0 (edge of the rhombus), and its angle, $\alpha(S_i, S_k)$, as

$$R_{\text{NNN}} = 2 \left(R_0^{\text{HL}} + \frac{\delta R}{4}(S_i + S_k) \right) \cos \frac{1}{2} \alpha(S_i, S_k), \quad (3)$$

$$R'_{\text{NNN}} = 2 \left(R_0^{\text{HL}} + \frac{\delta R}{4}(S_i + S_k) \right) \sin \frac{1}{2} \alpha(S_i, S_k). \quad (4)$$

We have to mention that the symmetry of the unit cell is decided based on the spin, S_k , of the site k regardless of the spins of the nearest neighbors j and l (refer to the schematic view of Fig. 1). That is why, in the Hamiltonian, the angle $\alpha(S_i, S_k)$ is spin dependent and its expression is written in a similar form as the bond length R_0 , given in Eq. (2):

$$\alpha(S_i, S_k) = \alpha_{\text{HL}} + \frac{\delta \alpha}{4}(S_i + S_k), \quad (5)$$

where $\delta \alpha = \alpha_{\text{HH}} - \alpha_{\text{LL}}$ is the angle misfit between the HS and LS states, the respective expressions of which are $\alpha_{\text{HH}} = \alpha(+1, +1)$ and $\alpha_{\text{LL}} = \alpha(-1, -1)$. $\alpha_{\text{HL}} = \alpha(-1, +1) = \alpha(+1, -1)$ is fixed for simplicity as $\alpha_{\text{HL}} = \frac{\alpha_{\text{HH}} + \alpha_{\text{LL}}}{2}$. In Eq. (1), A (respectively B) denotes the bond stiffness of NN (respectively NNN) in the lattice and $r_{ij} = \|\vec{r}_i - \vec{r}_j\|$ (respectively d_{ik} or d_{jl}) is the instantaneous distance between two NN (respectively NNN) sites. The quartic potential leads to different orientations of the cell in the HS state, i.e., the cell may stretch horizontally to the left or to the right or vertically upwards or downwards, which generates an important structural degeneracy.

The lattice (spins and positions) is evaluated in a multi-iterative approach as follows: for a site i , randomly selected, with spin ($S_i = \pm 1$) and position \vec{r}_i , a new spin value $S_i (= -S_i)$ will be set without position change. This spin change is accepted or rejected by the usual Metropolis criterion. Whatever the result emerging from the last step, the lattice is allowed to relax mechanically based on Monte Carlo procedure. Afterward, a new site is selected randomly and so on. Once all the nodes of the lattice are inspected for the spin change, we define such a step as the unit of Monte Carlo (MCS).

In the present model, we used the following parameter values derived from experimental data. The ligand-field energy is considered as $\Delta = 1200$ K and the degeneracy ratio $g = 150$ [55,71,72] leading to a molar entropy change at the transition $\Delta S = R \ln g = 82 \text{ J K}^{-1} \text{ Mol}^{-1}$ (R being the ideal gas constant) and a transition temperature, $T_{\text{eq}} = \frac{\Delta}{k_B \ln g} \approx 240$ K. The values of the NN equilibrium distances in the LS and HS states are independent of the bonds angles α and are respectively fixed to $R_0(-1, -1) = 1$ nm and $R_0(+1, +1) = 1.2$ nm, while for the HL state we consider $R_0(+1, -1) = \frac{[R_0(+1, +1) + R_0(-1, -1)]}{2} = 1.1$ nm. In contrast, the equilibrium NNN distances depend on α , so that if we consider now, for example, $\alpha_{\text{HH}} = \alpha(+1, +1) = 80^\circ$, the equilibrium bond lengths for the short and long diagonals are $d_0^- \approx 1.54$ nm and $d_0^+ \approx 1.83$ nm, respectively. However, in the LS state, the NNN equilibrium distance has only one value $\sqrt{2}R_0(-1, -1) \approx 1.4$ nm due to the cubic symmetry of the cell.

The used values of the elastic constants connect to Brillouin scattering experiments done on a single crystal of $[\text{Fe}(\text{ptz})_6](\text{ClO}_4)_2$ reported in [73] and prior works [74,75], which led to a bulk modulus, E , in the range 5–20 GPa. An estimation of the elastic constant A could be obtained by considering the elongation of a cubic cell using a 3D lattice, with a lattice parameter a , submitted to uniaxial stress. By neglecting the transversal effects, this simplified model results in the (approximate) relationship $A + 2B \approx Ea$. Following these observations, we find $A \approx 20\,000 \text{ K/nm}^2 \approx 20 \text{ meV/\AA}^2$, leading to the bulk modulus value, $E \approx 5$ GPa, which is in good agreement with the experimental data of literature.

III. RESULTS AND DISCUSSION

Initially, the lattice was prepared in the square-shaped LS state at 1 K, then warmed up to 500 K and cooled down to 1 K with a thermal step of 1 K. At each temperature step, 1000 MCS are taken to equilibrate the lattice and 1000 MCS are used for the statistics. To evaluate the effect of the structural degeneracy of the HS state on the thermal spin transition, different stretching angles of the HS cell were considered in the range $\alpha_{\text{HH}} \in [45^\circ - 90^\circ]$. During the thermal loop, the spin switching was monitored through the HS fraction, n_{HS} , and the average NN bond length, $\langle R \rangle$, defined respectively as

$$n_{\text{HS}} = \frac{(1 + \langle S_i \rangle)}{2} \quad (6)$$

and

$$\langle R \rangle = \frac{\sum_{ij} \sqrt{(x_i - x_j)^2 + (y_i - y_j)^2}}{\frac{N_b}{2}}, \quad (7)$$

where N_b is the total number of bonds between the NN i and j of respective coordinates (x_i, y_i) and (x_j, y_j) .

A. Thermal hysteresis

During this first study, the elastic constants A and B were kept constant as 20000 K/nm^2 and 20000 K/nm^4 , respectively, while we changed the values of α_{HH} . The system exhibits a first-order transition with hysteresis as illustrated in Figs. 2(a)–2(c) and SM 1 [76]. As the stretching angle α_{HH} increases the thermal loops are getting narrowed

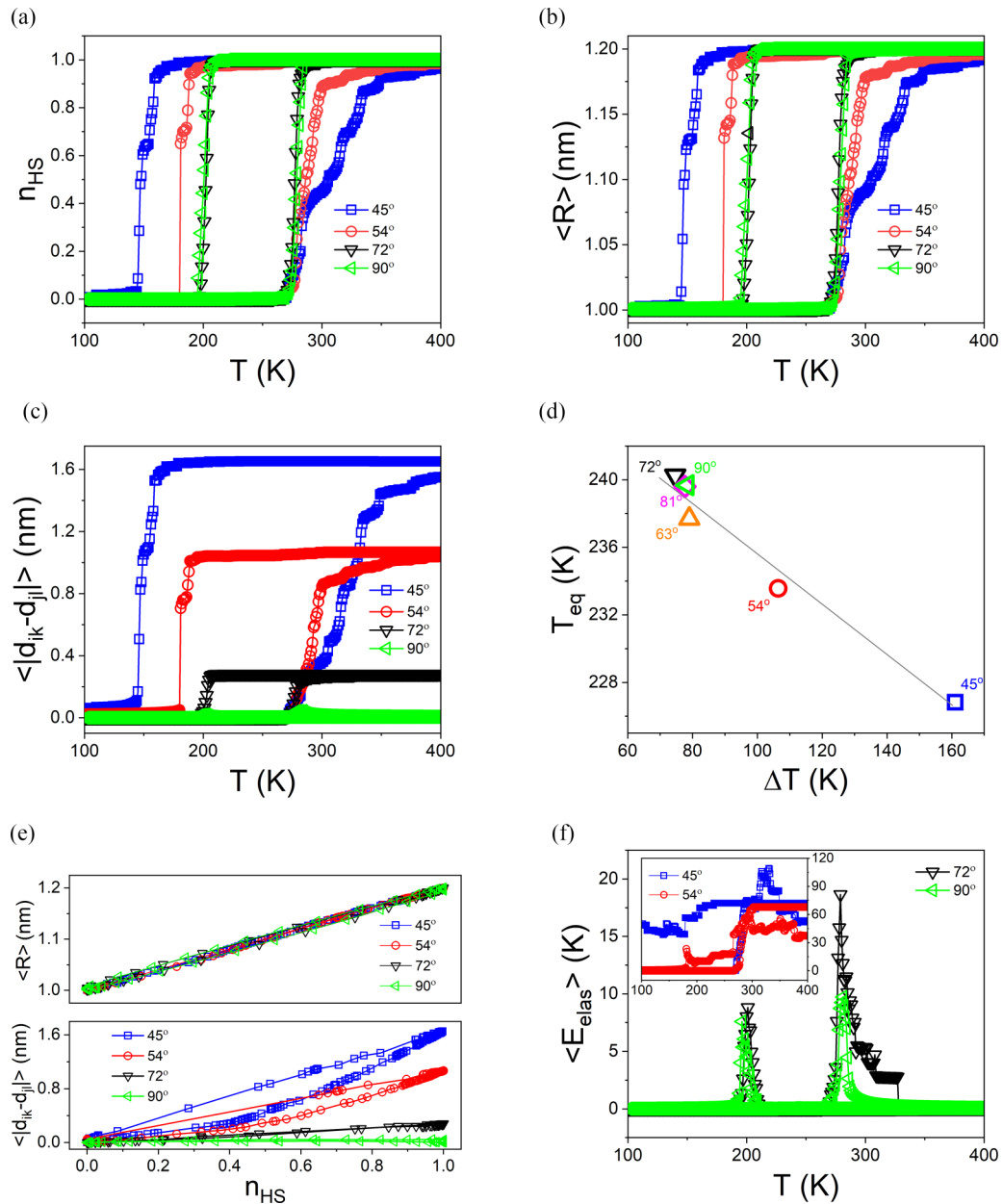


FIG. 2. Thermoinduced spin transition for different HS stretching angles, α_{HH} , monitored through (a) the HS fraction, n_{HS} , (b) the average lattice parameter, $\langle R \rangle$, and (c) the average absolute value of the diagonals' difference $\langle |d_{ik} - d_{jl}| \rangle$. (d) The transition temperature T_{eq} as a function of the width ΔT of the hysteresis loop. (e) bottom (respectively top) The correlation between the HS fraction and $\langle |d_{ik} - d_{jl}| \rangle$ (respectively $\langle R \rangle$). (f) Evolution of the density of elastic energy upon the transition for $\alpha_{\text{HH}} = 72^\circ$ and 90° . Inset: same but for $\alpha_{\text{HH}} = 45^\circ$ and 54° .

until they almost overlap. The analysis of the thermal hysteresis loops suggests that lowering α_{HH} stabilizes the HS phase on cooling, leading to larger hysteresis loops. The change of the equilibrium temperature T_{eq} , defined as $T_{\text{eq}} = \frac{T_{\text{HS} \rightarrow \text{LS}} + T_{\text{LS} \rightarrow \text{HS}}}{2}$, is correlated with the change in the width of the hysteresis loop as α_{HH} varies [see Fig. 2(d)]. The transition temperature $T_{\text{HS} \rightarrow \text{LS}}$ shifts significantly towards the lower temperatures, while the transition temperature of the heating branch, $T_{\text{LS} \rightarrow \text{HS}}$, remains almost unchanged. The latter kept almost the same value, except for $\alpha_{\text{HH}} = 45^\circ$, where a small step appears around $n_{\text{HS}} = 0.5$. This behavior will be investigated in detail later in the manuscript.

Indeed, the symmetry breaking upon the spin transition towards the HS state is confirmed by the thermal dependence of the average cell's diagonals' difference, $\langle |d_{ik} - d_{jl}| \rangle = \langle \sqrt{(d_{ij} - d_{jl})^2} \rangle$, over the lattice [see Fig. 2(c)]. Figure 2(e) confirms the existence of a perfect linear correlation between the magnetic response and the average NN structural bond length, $\langle R \rangle$, where a clear departure appears with Δd along the heating branch.

The interesting point emerging from Fig. 2 is the asymmetric dependence of the hysteresis loops with respect to the variation of α_{HH} , i.e., lattices presenting a strong anisotropy (lower values of α_{HH}) do not behave in the same way during

high-symmetry \rightarrow low-symmetry and low-symmetry \rightarrow high-symmetry transitions. This tendency is similar to the recent results reported by Ndiaye *et al.* [62], where the symmetry breaking was introduced by adjusting the misfit of elastic constants and bond lengths between the HS and LS states.

In Fig. 2(f), we monitored the thermoinduced spin transition for the different angles α_{HH} in terms of the average elastic energy. One can easily see that, if the symmetry of the LS state is close to that of the HS state ($\alpha_{\text{HH}} \in [72^\circ-90^\circ]$), the elastic energy peaks only along the heating and cooling branches. However, for the cases with strong symmetry breakings ($\alpha_{\text{HH}} < 72^\circ$), the deformation induced by the nucleation of HS sites generates configurations with higher energy even in a quasisaturated HS lattice [see inset in Fig. 2(f)].

In order to look more closely at the dynamic of the present spin transition, we investigated the spatiotemporal aspects of the thermoinduced HS \leftrightarrow LS switching for $\alpha_{\text{HH}} = 45^\circ$ and $\alpha_{\text{HH}} = 90^\circ$, the results of which are reported in Figs. 3 and 4, as well as in Figs. SM 2–5 [76]. For $\alpha_{\text{HH}} = 45^\circ$, it is clear that the lattice undergoes a transition from a high-symmetry LS state (a perfectly regular shape with squared cells) to a structurally “disordered” HS state. Indeed, as stated above, due to the quartic potential in the Hamiltonian of Eq. (1), the HS lattice’s cells might have several orientations. Consequently, the configurations of the lattice containing HS sites are quite degenerate and the number of complexions depends on the number of cells in the lattice. The coexistence of the different orientations generates a remarkable gliding of the atomic planes as could be seen in the heating branch of $\alpha_{\text{HH}} = 45^\circ$ [see Fig. 3(a)] and increases the elastic energy of the lattice [see the mappings of Fig. 3(c)].

The transition from the LS to HS state implies an important deformation for both cases with and without symmetry breaking. Such a structural transformation could be easily triggered from the lattice’s corners, thanks to the lack of neighboring cells involved in the transition. For the spin transition with symmetry breaking, if we consider a LS cell on one corner of the lattice, where the lattice shifts from the square-shaped towards diamond-shaped cells, the stretch of the latter along the free diagonal costs considerably less energy than the opposite diagonal. Then, the cells on the lattice’s borders are energetically more favorable to a structural change than those located in the center. Accordingly, for a cooperative lattice, the nucleation of the HS state from the center of the lattice is a rare event. De facto, we can imagine that the left upper corner of the lattice could stretch easily to the left side and upwards than to the right side and downwards. Such a germ of the stable phase may strongly impact the spatiotemporal aspects of the spin switching in the lattice, where the neighboring cells will stretch according to the symmetry of the first germ. However, the situation is a bit tricky and less straightforward than we can imagine, since the long-range character of the interactions is highly dependent on the structural anisotropy. The key aspect of this study is the structural multidomains feature, where the orientation of some cells in the center of the lattice could be trapped between different symmetries, which induces the waving configurations of the HS lattice and generates particular structural self-organization

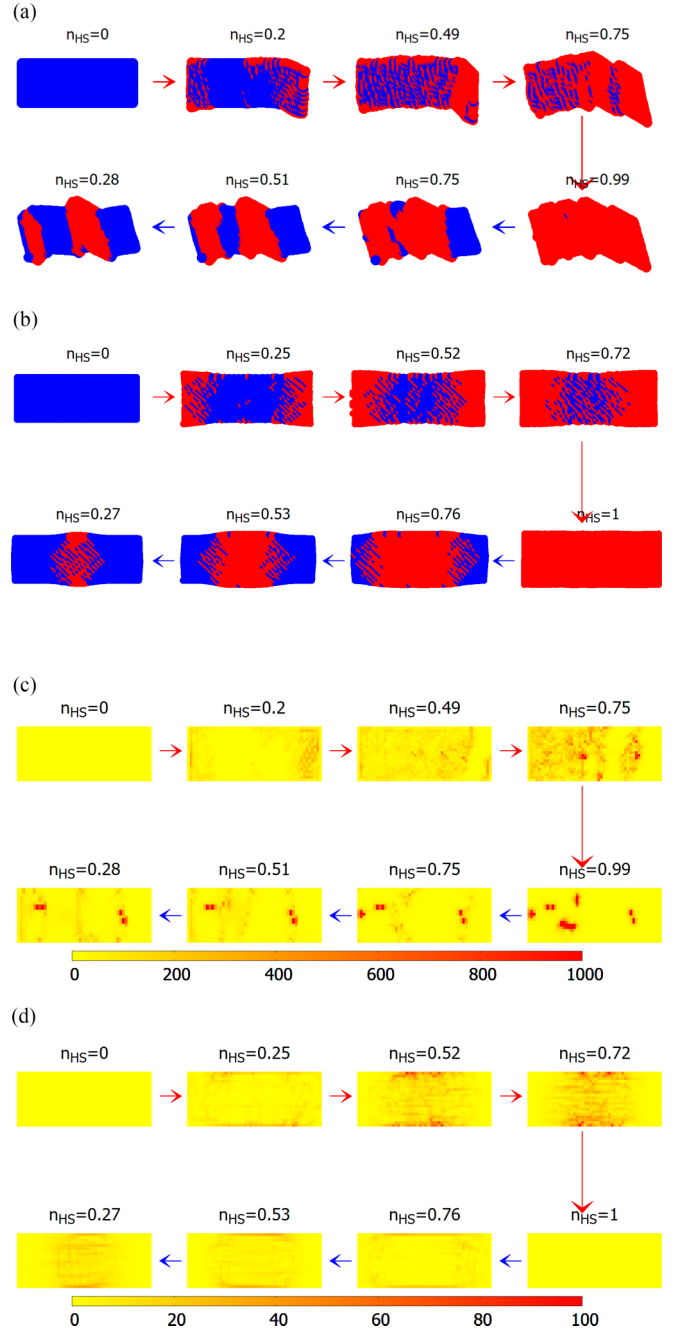


FIG. 3. Spatiotemporal aspects of the thermoinduced spin transition for (a) $\alpha_{\text{HH}} = 45^\circ$ and (b) $\alpha_{\text{HH}} = 90^\circ$. Red (blue) dots correspond to HS (LS) nodes. The corresponding mappings of the elastic energy upon the transition for (c) $\alpha_{\text{HH}} = 45^\circ$ and (d) $\alpha_{\text{HH}} = 90^\circ$. Note that in the mappings the scales of the color bar are different between the two angles. The mappings of the elastic energy are presented in the (i, j) referential, while lattice configurations are presented in the (x, y) referential. Red (blue) arrows correspond to the heating (cooling) process.

with higher elastic energy. In Fig. 3(a), we report the lattice configurations for $\alpha_{\text{HH}} = 45^\circ$ upon heating and cooling processes. The difference in behavior between the two branches is quite remarkable, where on heating a multidroplet character was observed unlike the multidomains feature

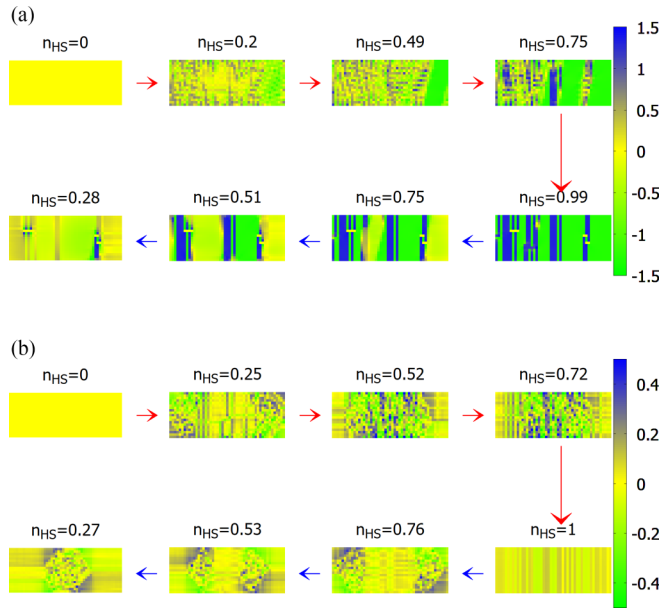


FIG. 4. Mappings of the diagonals' difference through the thermal spin transition for (a) $\alpha_{HH} = 45^\circ$ and (b) $\alpha_{HH} = 90^\circ$. Note that in the mappings the scales of the color bar are different between the two angles. The mappings are presented in the (i, j) referential. Red (blue) arrows correspond to the heating (cooling) process.

on cooling. Indeed, with its multidegenerated structural orientations, the lattice symmetry is remarkably lowered through the symmetry breaking, which also induces an important elastic anisotropy in the lattice which weakens the intermolecular interactions between sites in different directions. This anisotropy is at the origin of the asymmetric shift of the thermal loops reported in Figs. 2(a)–2(c), where the LS \rightarrow HS branches are almost superimposed, unlike the cooling branches which shift towards the lower temperatures. The difference in behavior between the cooling and heating processes depends on the value of α_{HH} , which controls the strength of the symmetry breaking, as well as on the temperature. In Fig. 3(b), we reported the spatiotemporal aspects of the spin transition for $\alpha_{HH} = 90^\circ$. In the latter case, the lattice is isotropic in both states ($\alpha_{HH} = \alpha_{LL}$), which suppresses the previous structural degenerescence observed for $\alpha_{HH} \neq \alpha_{LL}$. We should mention here that the latter case recalls earlier results obtained with microscopic simulations without symmetry breaking [56,57,66,77–85]. Such a fact justifies the similarity in the spatiotemporal aspects observed on both branches of cooling and heating, illustrated in Fig. 3(b), where two domains started to grow from all lattice corners and propagate toward the center. Moreover, the distribution of the elastic energy for the latter is quite similar in the heating and cooling branches [Fig. 3(d)].

B. Structural order vs structural disorder

Figures 4(a) and 4(b) report the corresponding spatial mapping of the diagonals' difference, $\Delta d = d_{ik} - d_{jl}$, for the two cases reported above $\alpha_{HH} = 45^\circ$ and $\alpha_{HH} = 90^\circ$. The different orientations of the cells can be easily distinguished by the blue (respectively green) color for the positive (respectively

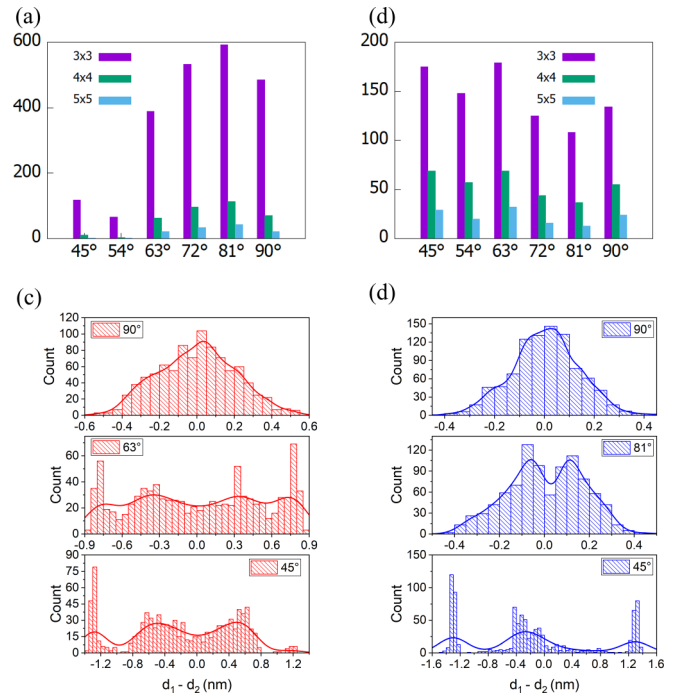


FIG. 5. Number of clusters of different sizes at $n_{HS} = 0.5$ for the different angles α_{HH} in the heating (a) and cooling (b) processes. Histograms showing the distribution of the diagonals' difference on the mapping of $(d_{ik} - d_{jl})$ at $n_{HS} \approx 0.5$ in heating (c) and cooling (d) processes for different angles α_{HH} .

negative) values. For example, for the cooling branch corresponding to $\alpha_{HH} = 45^\circ$, one can easily identify at $n_{HS} = 0.75$ the coexistence of small ordered structural domains trapped between the disordered HS and LS phases, which recall the experimental results of the two-step SCO complex $[Fe(2-pic)_3]Cl_2EtOH$ [42]. However, in the heating branch, such an observation is not straightforward due to thermal fluctuations. It is also interesting to stress the alternation of the structural domains observed in the configuration $n_{HS} = 0.99$, which explains the shape of the lattice reported in Fig. 3(a). These mappings may reveal the underlying mechanisms behind the nucleation and growth of the spin domains. In fact, at the interface between two structural domains (blue and green), some cells could be trapped with in-between symmetries (the yellow area), because they are subject to antagonist stresses. These trapped cells are potential sites for the nucleation of the LS state, since between the cells stretched towards one direction and those stretched towards other directions the unit cells might have a squared symmetry as that of the LS phase. That is to say, the nucleation of the LS state from the center of the lattice might be possible even before the nucleation in the lattice's edges, as could be seen in Figs. SM 2 and SM 3 [76] for the configurations $n_{HS} = 0.78$ and $n_{HS} = 0.9$ of the angles 54° and 63° , respectively. Due to the absence of symmetry breaking for the case $\alpha_{HH} = 90^\circ$, the magnitude of the diagonals' difference is relatively less important. Nevertheless, here too, the mappings reveal the effect of thermal fluctuations on the lattice in the heating branch, where it is difficult to identify the macroscopic spin domains of Fig. 3(b), unlike in the cooling branch.

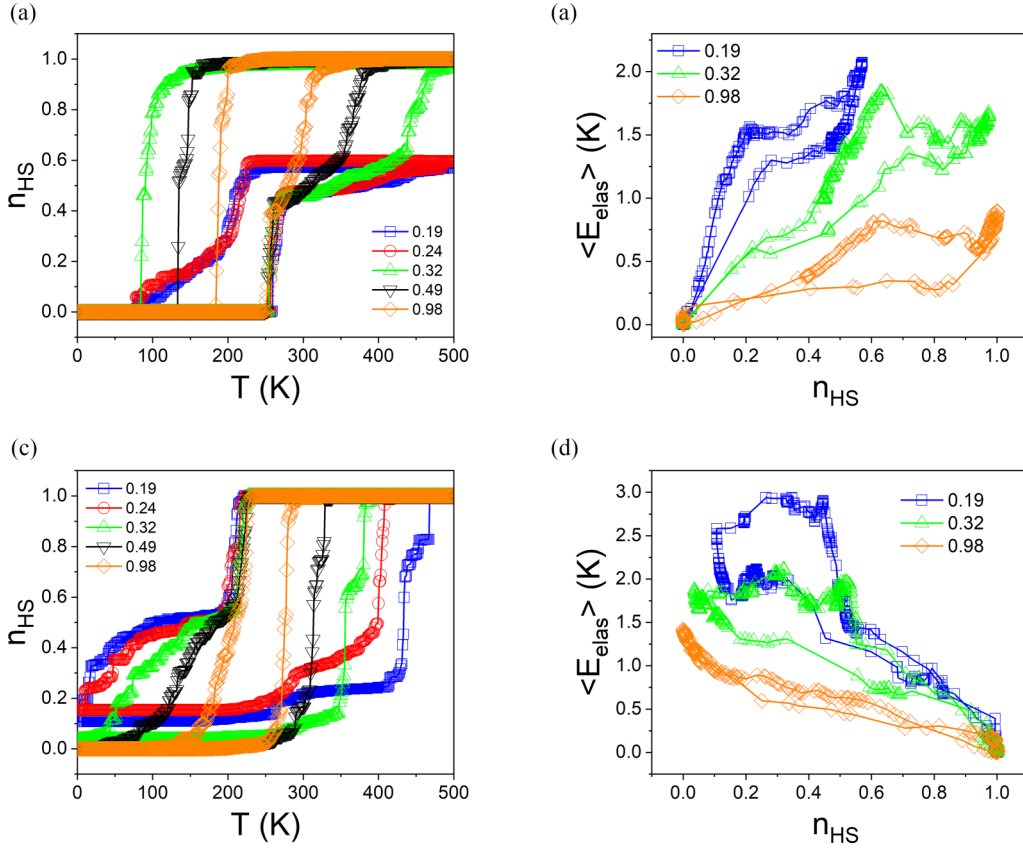


FIG. 6. (a) Thermoinduced spin transition between a high-symmetry LS state and a low-symmetry HS state for different elastic energy ratios E_{NN}/E_{NNN} , where E_{NN} (respectively E_{NNN}) is the elastic energy due to the interactions with the nearest neighbor NN (respectively NNN). (b) The corresponding average elastic energy through the spin transition for the different energy ratios reported in (a). (c) Thermoinduced spin transition for different energy ratios E_{NN}/E_{NNN} between a high-symmetry HS state and a low-symmetry LS state. (d) The corresponding average elastic energy through the spin transition for the different energy ratios reported in (c).

C. Quantitative investigation

For a comprehensive analysis, the spatiotemporal aspects obtained with the different angles were quantitatively investigated to build a comparative approach that can distinguish subtleties of self-organization of spin domains. Figures 5(a) and 5(b) show histograms corresponding to the number of spin clusters of different sizes 3×3 , 4×4 , and 5×5 cells determined at $n_{HS} = 0.5$ for the different angles α_{HH} in the heating and cooling processes, respectively. For the angles in the interval $[72^\circ - 90^\circ]$, the distribution of spin domains is almost homogeneous in the heating and cooling processes in agreement with the symmetrical shape of the thermal loops shown in Fig. 2. On the other hand, the number of clusters for the cases with a strong symmetry breaking (lower values of α_{HH}) shows a remarkable difference in the two branches of the thermal loop, where the asymmetry in behavior between $LS \rightarrow HS$ and $HS \rightarrow LS$ is enhanced. For example, for $\alpha_{HH} = 45^\circ$, the number of clusters 5×5 increased from 1 in heating to 29 in cooling.

Furthermore, in Figs. 5(c) and 5(d) we studied the frequency distribution of the diagonals' difference over the mappings $d_{ik} - d_{jl}$ at $n_{HS} = 0.5$ for the different angles. For example, for $\alpha_{HH} = 90^\circ$, one can easily see that both distributions in heating and cooling are centered around zero due

to the absence of symmetry breaking in this case. However, due to the thermal fluctuation, the standard deviation of the distribution in heating ($\sigma_{heating} = 0.2$) is larger than the one in cooling ($\sigma_{cooling} = 0.13$). As the symmetry breaking is getting stronger (i.e., α_{HH} decreases), the distributions gradually split into components corresponding to the different orientations of the unit cells. For $\alpha_{HH} = 45^\circ$, the histograms in cooling show three peaks, corresponding to the number of cells stretched to the right, to the left, and the ones trapped in between. The diagonals' difference for the latter concentration is around zero. We should mention here that it is slightly more difficult to identify the different orientations of the cells from the histograms determined on the heating branch.

D. Synergy between elastic interactions

The plateau observed in the heating branch of the thermal hysteresis loop of $\alpha_{HH} = 45^\circ$ around $n_{HS} = 0.5$ (Fig. 2) is most likely linked to the synergy between the elastic terms of Hamiltonian (1). Therefore, in the following, we will investigate this effect. To do so, we studied the thermoinduced spin transition for different ratios of NN and NNN contributions of the elastic energies, $\frac{E_{NN}}{E_{NNN}}$, for $\alpha_{HH} = 45^\circ$. In this subsection, we changed the lattice parameters to make the energies E_{NN}

and E_{NNN} more comparable as for the results presented above where the ratio $\frac{E_{\text{NNN}}}{E_{\text{NN}}} \approx 3.6$. Thus we reduced the mismatch of lattice parameters between the HS and LS states from 0.2 nm to 0.1 nm, where the new values are $R_0^{\text{HH}} = 1.1$ nm and $R_0^{\text{LL}} = 1$ nm, while keeping $R_0^{\text{HL}} = \frac{R_0^{\text{HH}} + R_0^{\text{LL}}}{2}$. The ratio $\frac{E_{\text{NNN}}}{E_{\text{NN}}}$ is monitored by varying the NNN elastic constant B in the range [4000–20000] K/nm⁴, while keeping $A = 20\,000$ K/nm² constant. Accordingly, the ratio $\frac{E_{\text{NNN}}}{E_{\text{NN}}}$ is in the range [0.19–0.98]. For these different values, we investigated the thermoinduced spin transition, the results of which are summarized in Fig. 6(a). As the weight of E_{NNN} increases with respect to E_{NN} , the energy barrier increases and the system undergoes a partial spin transition, where $\approx 50\%$ of the lattice remains trapped in the LS state at higher temperatures as could be seen for the ratios $\frac{E_{\text{NNN}}}{E_{\text{NN}}} = 0.19$ and $\frac{E_{\text{NNN}}}{E_{\text{NN}}} = 0.24$. Figure 6(b) shows the evolution of the density of the elastic energy alongside the thermal hysteresis loops for the three cases $\frac{E_{\text{NNN}}}{E_{\text{NN}}} = 0.19, 0.32,$ and 0.98 . We should stress that, if the value of E_{NNN} is strong compared to E_{NN} , the lattice cannot evacuate easily the excess of elastic energy, which explains the shape of the curve corresponding to $\frac{E_{\text{NNN}}}{E_{\text{NN}}} = 0.19$. Therefore, more structural frustrations will appear locally and the whole lattice is very heterogeneous. Consequently, the lattice is storing an important amount of elastic energy that hinders the complete spin transition [81]. On the other hand, as E_{NNN} approaches E_{NN} , the mechanical features of the lattice are homogeneous and the excess of elastic energy due to the spin transition is released easily through the lattice. Hence the density of elastic energy is considerably lowered as can be seen in Fig. 6(b) for $\frac{E_{\text{NNN}}}{E_{\text{NN}}} = 0.98$.

The spatiotemporal aspects of the spin transition for the different ratios $\frac{E_{\text{NNN}}}{E_{\text{NN}}}$ are quite similar to the ones reported in Fig. 3(a). The snapshots corresponding to the ratios 0.32 and 0.98 are illustrated in Fig. 7(a) and in Fig. SM 6 [76], respectively. For both cases, we notice that the nucleation and growth of the LS state on cooling is more cooperative than the case shown in Fig. 3(a), where the system tends to develop single domains of HS and LS phases. On the other hand, the snapshots on heating reveal an interesting labyrinthlike self-organization with an alternation of HS and LS layers, which recall the results reported on the SCO system $Fe[HC(3, 5 - Me_2pz)_3](BF_4)_2$, where $HC(3, 5 - Me_2pz)_3 = \text{scorpionatelike tridentate ligand}$ and $tris(3, 5 - \text{dimethyl} - 1 - \text{pyrazolyl})\text{methane}$ [46]. Indeed, the mapping of elastic energy over the lattice through the thermoinduced spin transition, reported in Fig. 7(c), confirms the impact of thermal fluctuations, where in the heating process the excess of the elastic energy is distributed over the whole lattice. However, in the cooling branch, there exists some areas with higher elastic energy contrasting with the rest of the lattice. By taking the snapshots of Fig. 7(a) as a reference, it is easy to link those areas of higher elastic energy to the domain boundaries, where the important mismatch of lattice parameters is at the origin of the excess of elastic energy.

The corresponding mapping of the diagonals' difference, $(d_{ik} - d_{jl})$, for the ratio $\frac{E_{\text{NNN}}}{E_{\text{NN}}} = 0.32$, is reported in Fig. 8(a). In the saturated LS state, where all lattice bond lengths reach their equilibrium values, the latter quantity is null. However, for $n_{\text{HS}} = 0.97$, it evolves between 1.5 nm and -1.5 nm,

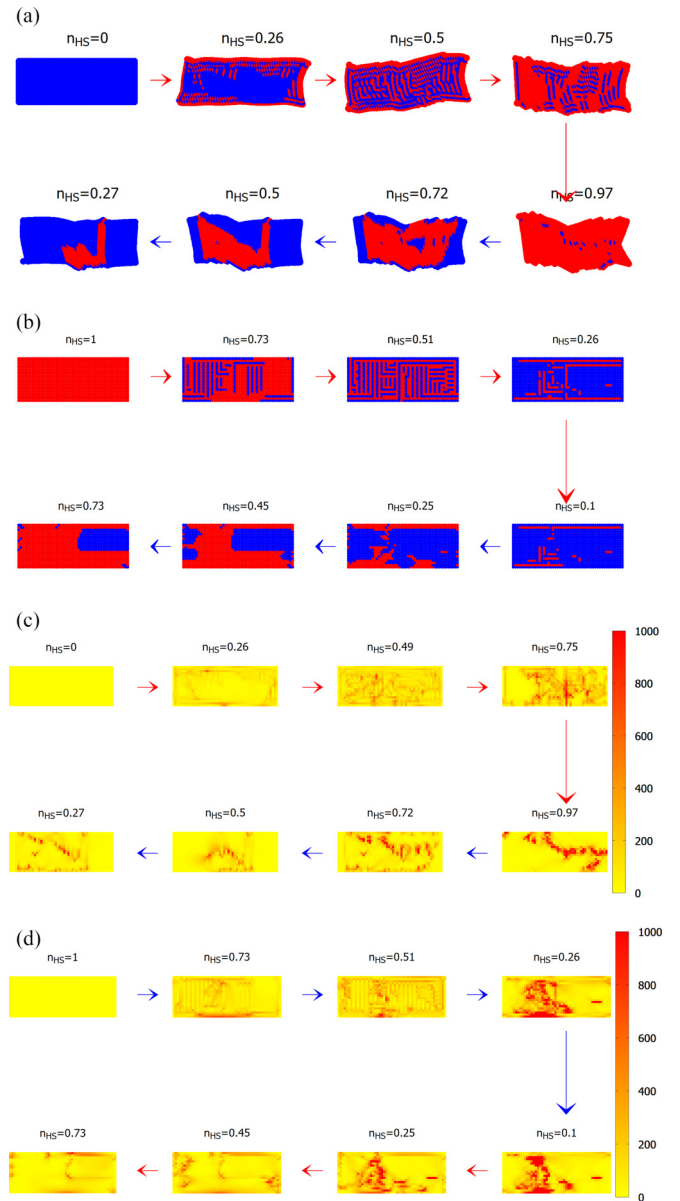


FIG. 7. Spatiotemporal aspects of the thermoinduced spin transition (a) between a high-symmetry LS state and a low-symmetry HS state with $\frac{E_{\text{NNN}}}{E_{\text{NN}}} = 0.32$ and (b) between a high-symmetry HS state and a low-symmetry LS state with $\frac{E_{\text{NNN}}}{E_{\text{NN}}} = 0.19$. Panels (c) and (d) are respectively the corresponding mappings of the elastic energy for the configurations of (a) and (b). Red (blue) arrows in the sketches correspond to the heating (cooling) process.

which corresponds to the blue and green colors, respectively. Such a mapping highlights once again the difference in the dynamics between the heating and the cooling processes of the thermal hysteresis LS \rightarrow HS phases and vice versa. In the heating regime, no macroscopic structural domains (having the same cell's orientation, i.e., stretched to the right or to the left) were observed, unlike the cooling process. Such an asymmetry is due to the difference in the starting configurations of both processes, which are obviously not the same. The saturated LS state is a homogeneous lattice, where all of the cells are perfectly squared [see Fig. 8(a) for $n_{\text{HS}} = 0$].

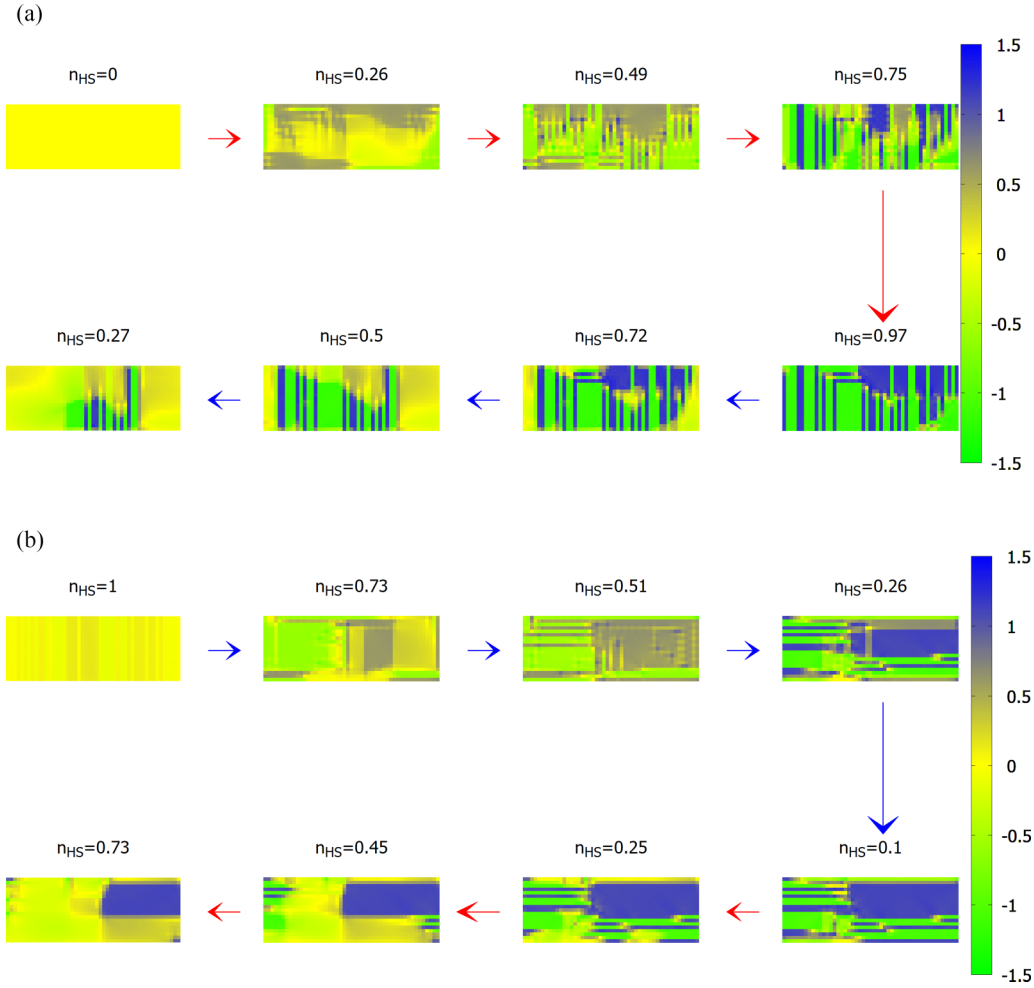


FIG. 8. Panels (a) and (b) are respectively the corresponding mappings of the diagonals' difference for the configurations (a) and (b) of Fig. 7. Red (blue) arrows in the sketches correspond to the heating (cooling) process.

In contrast, on cooling, the transition starts from a HS lattice with a mixture of cells stretched to the right, left, upward, and downward.

The shape of the lattice plays a crucial role in the self-organization of the structural domains due to the long-range character of the elastic interactions. Most likely, the domains spread along the shortest side because it involves fewer nodes to displace. The intersection of structural domains with different orientations traps structurally metastable configurations [Fig. 8(a), $n_{\text{HS}} = 0.49$], which are behind the step observed in the hysteresis loop of Fig. 6(a).

Moreover, the mappings of the diagonals' difference show the effect of the structural anisotropy on the long-range character of the interactions. For example, for the configuration of $n_{\text{HS}} = 0.97$, the comparison between the maps of elastic energy, reported in Fig. 7(c) and of the diagonals' difference in Fig. 8(a) reveals that the elastic energy peaks at the intersections of two or more domains of different structural orientations. These are regions of high elastic stress. In contrast, two adjacent structural domains do not generate a huge amount of elastic energy and can efficiently relax the structural stress. The self-organization of the lattice into several

structural domains in cooling contrasts with the multidroplet nucleation of the HS state during the heating process.

E. Symmetry breaking while switching between a cubic HS state and a diamond LS state

We investigated as well in the opposite situation where the symmetry breaking occurs from a cubic HS state ($\alpha_{\text{HH}} = 90^\circ$), while switching to the LS state, i.e., $\alpha_{\text{LL}} = 45^\circ$. For this part, we used the same values of lattice parameters and elastic constants as in the previous subsection, where we considered the same ratios of elastic energy as above. The corresponding thermal hysteresis loops for this simulation are illustrated in Fig. 6(c); a significant difference in the shape of the loops is noticed compared to Fig. 6(a). Here, we invite the reader to consult Fig. SM 7 [76] for the individual comparison of each thermal loop. For $\frac{E_{\text{NN}}}{E_{\text{NNN}}} < 0.49$, multisteps were observed in both branches of the hysteresis loop. In fact, for the ratios $\frac{E_{\text{NN}}}{E_{\text{NNN}}} = 0.32$ and 0.19 , the system struggles to undergo a complete spin transition, as it still shows difficulties switching all the molecules into the LS state at lower temperatures, where a non-null residual HS fraction was observed in Fig. 6(c). By

referring to Fig. 6(a), we recall that the transition in the two latter ratios was as well incomplete. Here again, this incompleteness is due to the large amount of elastic energy stored in the system that cannot be released easily due to the misfit of the elastic parameters between the nearest and next-nearest neighbors.

Figure 6(d) shows the average elastic energy over the lattice for the thermal hysteresis loops of Fig. 6(c). The latter increases as the disorder increases in the lattice, in good agreement with Fig. 6(b). Indeed, the evolution of the elastic energy, through the spin transition, confirms that the structural frustration introduced by the symmetry breaking increases the elastic energy. That is particularly true in the cooling branches of the thermal transitions, around the switching temperatures, where the thermal fluctuations are relatively low. The latter fact tells us that the dynamic of the spin transition with symmetry breaking is dependent on the thermal history. Starting from a cubic LS phase at lower temperatures, the thermal fluctuations in the heating branch generate more structural frustrations, which traps several LS sites and justifies the incomplete transition observed with the ratios $\frac{E_{\text{NN}}}{E_{\text{NNN}}} = 0.19$ and 0.24 in Fig. 6(a). However, for a transition towards a cubic or high-symmetry phase at higher temperatures, the thermal fluctuations are useful to overcome the local structural traps due to the mechanical frustration of the lattice, which justifies the different steps observed in the heating branches in Fig. 6(c). The latter effect impacts as well the width of the thermal hysteresis, especially for the lower ratios $\frac{E_{\text{NN}}}{E_{\text{NNN}}}$. One can easily see that the width of the thermal loop of $\frac{E_{\text{NN}}}{E_{\text{NNN}}} = 0.19$ in Fig. 6(c) is almost doubled when compared to the one in Fig. 6(a).

As the ratio $\frac{E_{\text{NN}}}{E_{\text{NNN}}}$ gets important, both thermal loops in Figs. 6(a) and 6(c) show closer behaviors. The latter fact is confirmed as well for the $\frac{E_{\text{NN}}}{E_{\text{NNN}}} = 3.6$, reported in the subsections A–C, where the thermal loops were simulated for both scenarios: cubic HS state \leftrightarrow diamond LS state and cubic LS state \leftrightarrow diamond HS state. The individual comparisons in the latter simulation are reported in Fig. SM 8 [76]. For the diamond unit cell, we considered the same angles as earlier $\alpha \in [45^\circ - 90^\circ]$.

The largest hysteresis loop in Fig. 6(c) was obtained for the ratio $\frac{E_{\text{NN}}}{E_{\text{NNN}}} = 0.19$. The corresponding spatiotemporal aspects are reported in Figs. 7(b) and 7(d) and Fig. 8(b). The configurations of the lattice through the spin transition [Fig. 7(b)] remarkably contrast with those reported in Figs. 3 and 7(a). The alternations of HS and LS sites were observed in cooling upon switching from HS to LS, while the multidomains feature took place in heating along the LS \rightarrow HS transition. We have to mention that, for the latter case, the corresponding elastic energy E_{NNN} is particularly significant compared to E_{NN} , in such a way that the spin transition induces remarkable macroscopic lattice deformation. The mappings of the elastic energy as well as the diagonals' difference are consistent with the lattice configurations as could be seen in Fig. 7(d) and Fig. 8(b), respectively. Indeed, these figures evidence an interesting correlation between the spatial organization of the structural domains and the spin domains. Such a fact

highlights the decisive role of symmetry breaking in the cooperativity of the system.

IV. CONCLUSION

This paper tackled the problem of the interplay between a lattice symmetry breaking and a thermoinduced spin transition using a full elastic quartic potential acting on the NNN elastic interactions. The Hamiltonian proposed in this work generates different crystallographic orientations between HS and LS states transforming from diamond shaped cells to squared cells or vice versa. The rhombus shaped state is characterized by an important structural anisotropy, where several orientations of the unit cell may coexist. To stress out such an effect on the spin transition, in the case of a rhombus HS state, we considered different stretching angles of the HS unit cell and simulated the thermoinduced spin transition on a 2D lattice. We demonstrated that the symmetry breaking accompanying the electronic spin transition induces unsymmetrical hysteresis loops. We found that, as the stretching angle α_{HH} decreases from the ideal isotropic value ($\alpha_{\text{HH}} = 90^\circ$), a step appears on the heating branch at $n_{\text{HS}} = 0.5$ without changing the switching temperature, while the cooling branch shifts towards the lower temperatures. The spatiotemporal aspects corresponding to the symmetry breaking revealed a quite interesting self-organization of spin domains as an alternation of HS and LS layers in the heating process, as well as the presence of alternate structural domains of different orientations in the cooling branch. Furthermore, we investigated the effect of the energy competition between NN and NNN elastic interactions on the thermoinduced spin switching properties. We found that, if the values of elastic energies for the NN and NNN are close, the lattice releases easily the excess of elastic energy and undergoes a complete spin transition between the LS and HS states. Moreover, we demonstrated that, due to the symmetry breaking, the crossing of structural domains with different orientations traps structurally long-lived metastable configurations, which are at the origin of the step observed in the ascending branches of the thermal hysteresis loops. Such trapped and miscible phases, which do not have the structure of the majority phase, are potential nucleation sites of the new phase. Overall, the asymmetric character of the thermal hysteresis emerging from the structural symmetry breaking effects leads to observing spatiotemporal features of spin transition which are sensitive to the thermal history of the lattice, where a multidroplet nucleation mechanism takes place in the heating process, while a multidomain growth emerges in the cooling branch. Accordingly, it is clear that the symmetry breaking perturbed the long-range interactions along the lattice and that was further enhanced with the thermal fluctuations, which justifies the multidroplet nucleation of the HS sites. We have to stress that most of the cases treated here reproduce well experimental facts, which pave the way to a further understanding of the intimate microscopic couplings between the electronic degrees of freedom and the structural transformation. On the basis of the findings presented here, further study of the effect of the size and shape of the lattice

on the thermo- and photoinduced spin transition is continuing and will be presented in future papers.

ACKNOWLEDGMENTS

The authors acknowledge the support received from the Ministry of Higher Education and Scientific Research of Tunisia, from Sorbonne University Abu Dhabi (project:

Microscopic simulation of structural degeneracy and its effect on the phase transition in molecular materials), CNRS (Centre National de la Recherche Scientifique) through the MITI interdisciplinary programs through its exploratory research program, the University of Versailles and Paris-Saclay, as well as the Agence Nationale de la Recherche (Project No. Mol-CoSM: ANR-20-CE07-0028-02).

There are no conflicts of interest to declare.

- [1] P. Gütllich and H. Goodwin, Spin crossover - an overall perspective, in *Spin Crossover in Transition Metal Compounds I*, Topics in Current Chemistry Vol. 233 (Springer, New York, 2004), pp. 1–47.
- [2] P. Gütllich, Spin crossover in iron(ii)-complexes, *Struct. Bonding* **44**, 83 (1981).
- [3] P. Gütllich, A. Hauser, and H. Spiering, Thermal and optical switching of iron(ii) complexes, *Angew. Chem., Int. Ed. Engl.* **33**, 2024 (1994).
- [4] E. König, Nature and dynamics of the spin-state interconversion in metal-complexes, *Struct. Bonding* **76**, 51 (1991).
- [5] O. Kahn and C. Martinez, Spin-transition polymers: From molecular materials toward memory devices, *Science* **279**, 44 (1998).
- [6] A. Bousseksou, K. Boukheddaden, M. Goiran, C. Consejo, M.-L. Boillot, and J.-P. Tuchagues, Dynamic response of the spin-crossover solid $\text{Co}(\text{H}_2(\text{fsa})_2\text{en})(\text{py})_2$ to a pulsed magnetic field, *Phys. Rev. B* **65**, 172412 (2002).
- [7] W. Kosaka, K. Nomura, K. Hashimoto, and S. Ohkoshi, Observation of an Fe(ii) spin-crossover in a cesium iron hexacyanochromate, *J. Am. Chem. Soc.* **127**, 8590 (2005).
- [8] D. Papanikolaou, W. Kosaka, S. Margadonna, H. Kagi, S.-i. Ohkoshi, and K. Prassides, Piezomagnetic behavior of the spin crossover Prussian blue analogue $\text{CsFe}[\text{Cr}(\text{CN})_6]$, *J. Phys. Chem. C* **111**, 8086 (2007).
- [9] F. Prins, M. Monrabal-Capilla, E. A. Osorio, E. Coronado, and H. S. J. van der Zant, Room-temperature electrical addressing of a bistable spin-crossover molecular system, *Adv. Mater.* **23**, 1545 (2011).
- [10] A. Bousseksou, F. Varret, M. Goiran, K. Boukheddaden, and J. Tuchagues, The spin crossover phenomenon under high magnetic field, in *Spin Crossover in Transition Metal Compounds III*, Topics in Current Chemistry Vol. 235 (Springer, Berlin Heidelberg, 2004), pp. 65–84.
- [11] C. Bartual-Murgui, A. Akou, C. Thibault, G. Molnár, C. Vieu, L. Salmon, and A. Bousseksou, Spin-crossover metal-organic frameworks: promising materials for designing gas sensors, *J. Mater. Chem. C* **3**, 1277 (2015).
- [12] J. Dugay, M. Giménez-Marqués, W. J. Venstra, R. Torres-Cavanillas, U. N. Sheombaring, N. Manca, E. Coronado, and H. S. J. van der Zant, Sensing of the molecular spin in spin-crossover nanoparticles with micromechanical resonators, *J. Phys. Chem. C* **123**, 6778 (2019).
- [13] C.-M. Jureschi, J. Linares, A. Boulmaali, P. Dahoo, A. Rotaru, and Y. Garcia, Pressure and temperature sensors using two spin crossover materials, *Sensors* **16**, 187 (2016).
- [14] P. Guionneau, M. Marchivie, G. Bravic, J.-F. Létard, and D. Chasseau, Structural aspects of spin crossover. example of the $[\text{Fe}^{\text{II}}\text{L}_n(\text{NCS})_2]$ complexes, in *Spin Crossover in Transition Metal Compounds II*, Topics in Current Chemistry, Vol. 234 (Springer, Berlin, Heidelberg, 2004), pp. 97–128.
- [15] M. Cammarata, R. Bertoni, M. Lorenc, H. Cailleau, S. Di Matteo, C. Mauriac, S. F. Matar, H. Lemke, M. Chollet, S. Ravy, C. Laulhé, J.-F. Létard, and E. Collet, Sequential Activation of Molecular Breathing and Bending during Spin-Crossover Photoswitching Revealed by Femtosecond Optical and X-Ray Absorption Spectroscopy, *Phys. Rev. Lett.* **113**, 227402 (2014).
- [16] M. A. Halcrow, Structure: function relationships in molecular spin-crossover complexes, *Chem. Soc. Rev.* **40**, 4119 (2011).
- [17] M. Lorenc, J. Hébert, N. Moisan, E. Trzop, M. Servol, M. Buron-Le Cointe, H. Cailleau, M. L. Boillot, E. Pontecorvo, M. Wulff, S. Koshihara, and E. Collet, Successive Dynamical Steps of Photoinduced Switching of a Molecular Fe(III) Spin-Crossover Material by Time-Resolved X-Ray Diffraction, *Phys. Rev. Lett.* **103**, 028301 (2009).
- [18] M. Buron-Le Cointe, J. Hébert, C. Baldé, N. Moisan, L. Toupet, P. Guionneau, J. F. Létard, E. Freysz, H. Cailleau, and E. Collet, Intermolecular control of thermoswitching and photoswitching phenomena in two spin-crossover polymorphs, *Phys. Rev. B* **85**, 064114 (2012).
- [19] K. Ridier, G. Molnár, L. Salmon, W. Nicolazzi, and A. Bousseksou, Hysteresis, nucleation and growth phenomena in spin-crossover solids, *Solid State Sci.* **74**, A1 (2017).
- [20] A. Slimani, F. Varret, K. Boukheddaden, C. Chong, H. Mishra, J. Haasnoot, and S. Pilet, Visualization and quantitative analysis of spatiotemporal behavior in a first-order thermal spin transition: A stress-driven multiscale process, *Phys. Rev. B* **84**, 094442 (2011).
- [21] A. Slimani, F. Varret, K. Boukheddaden, D. Garrot, H. Oubouchou, and S. Kaizaki, Velocity of the High-Spin Low-Spin Interface Inside the Thermal Hysteresis Loop of a Spin-Crossover Crystal, via Photothermal Control of the Interface Motion, *Phys. Rev. Lett.* **110**, 087208 (2013).
- [22] N. Bréfuel, E. Collet, H. Watanabe, M. Kojima, N. Matsumoto, L. Toupet, K. Tanaka, and J.-P. Tuchagues, Nanoscale self-hosting of molecular spin-states in the intermediate phase of a spin-crossover material, *Chem. Eur. J.* **16**, 14060 (2010).
- [23] N. Bréfuel, H. Watanabe, L. Toupet, J. Come, N. Matsumoto, E. Collet, K. Tanaka, and J.-P. Tuchagues, Concerted spin crossover and symmetry breaking yield three thermally and one light-induced crystallographic phases of a molecular material, *Angew. Chem., Int. Ed.* **48**, 9304 (2009).
- [24] M. Nishino, P. A. Rikvold, C. Omand, and S. Miyashita, Multistability in an unusual phase diagram induced by the competition between antiferromagnetic-like short-range and ferromagnetic-like long-range interactions, *Phys. Rev. B* **98**, 144402 (2018).
- [25] S. Zerdane, M. Cammarata, L. Balducci, R. Bertoni, L. Catala, S. Mazerat, T. Mallah, M. N. Pedersen, M. Wulff, K. Nakagawa, H. Tokoro, S.-i. Ohkoshi, and E. Collet, Probing transient photoinduced charge transfer in prussian blue analogues with

- time-resolved xanes and optical spectroscopy, *Eur. J. Inorg. Chem.* **2018**, 272 (2018).
- [26] B. Weber, C. Carbonera, C. Desplances, and J.-F. Létard, Stepwise spin transition in a mononuclear iron(II) complex with unusually wide plateau, *Eur. J. Inorg. Chem.* **2008**, 1589 (2008).
- [27] Y. Garcia, O. Kahn, L. Rabardel, B. Chansou, L. Salmon, and J. P. Tuchagues, Two-step spin conversion for the three-dimensional compound Tris(4,4'-bis-1,2,4-triazole)iron(II) diperchlorate, *Inorg. Chem.* **38**, 4663 (1999).
- [28] H. Watanabe, K. Tanaka, N. Bréfuel, H. Cailleau, J.-F. Létard, S. Ravy, P. Fertey, M. Nishino, S. Miyashita, and E. Collet, Ordering phenomena of high-spin/low-spin states in stepwise spin-crossover materials described by the ANNNI model, *Phys. Rev. B* **93**, 014419 (2016).
- [29] M. Paez-Espejo, M. Sy, and K. Boukheddaden, Elastic frustration causing two-step and multistep transitions in spin-crossover solids: Emergence of complex antiferroelastic structures, *J. Am. Chem. Soc.* **138**, 3202 (2016).
- [30] M. Itoi, I. Maurin, K. Boukheddaden, M. J. Andrus, D. R. Talham, E. Elkaim, and Y. Uwatoko, Sub-micrometer particle size effects on metastable phases for a photoswitchable co-fe prussian blue analog, *J. Appl. Phys.* **131**, 085110 (2022).
- [31] M. Seredyuk, K. Znovjyak, F. J. Valverde-Muñoz, M. C. Muñoz, I. O. Fritsky, V. M. Amirkhanov, and J. A. Real, Spin transition and symmetry-breaking in new mononuclear feII tren-complexes with up to 38 k hysteresis around room temperature, *Inorg. Chem. Front.* **9**, 537 (2022).
- [32] Y. Singh, K. Affes, N.-I. Belmouri, and K. Boukheddaden, Clamping of spin-crossover solid inducing crystal bending and spatial spin organization, *Mater. Today Phys.* **27**, 100842 (2022).
- [33] S. Pillet, Spin-crossover materials: Getting the most from x-ray crystallography, *J. Appl. Phys.* **129**, 181101 (2021).
- [34] S. Bedoui, G. Molnár, S. Bonnet, C. Quintero, H. J. Shepherd, W. Nicolazzi, L. Salmon, and A. Bousseksou, Raman spectroscopic and optical imaging of high spin/low spin domains in a spin crossover complex, *Chem. Phys. Lett.* **499**, 94 (2010).
- [35] E. M. Hernández, S. Zheng, H. J. Shepherd, D. S. Yufit, K. Ridier, S. Bedoui, W. Nicolazzi, V. Velázquez, S. Bonnet, G. Molnár, and A. Bousseksou, Spatially resolved investigation and control of the bistability in single crystals of the [Fe(bbpy)(NCS)₂] spin crossover complex, *J. Phys. Chem. C* **120**, 27608 (2016).
- [36] J. A. K. Howard and M. R. Probert, Cutting-edge techniques used for the structural investigation of single crystals, *Science* **343**, 1098 (2014).
- [37] K. Ridier, G. A. Craig, F. Damay, T. Fennell, M. Murrie, and G. Chaboussant, Probing photoinduced spin states in spin-crossover molecules with neutron scattering, *Phys. Rev. B* **95**, 094403 (2017).
- [38] Y. Jiang, L. C. Liu, H. M. Müller-Werkmeister, C. Lu, D. Zhang, R. L. Field, A. Sarracini, G. Moriena, E. Collet, and R. J. D. Miller, Structural dynamics upon photoexcitation in a spin crossover crystal probed with femtosecond electron diffraction, *Angew. Chem., Int. Ed.* **56**, 7130 (2017).
- [39] S. Pillet, E.-E. Bendeif, S. Bonnet, H. J. Shepherd, and P. Guionneau, Multimetastability, phototrapping, and thermal trapping of a metastable commensurate superstructure in a Fe^{II} spin-crossover compound, *Phys. Rev. B* **86**, 064106 (2012).
- [40] P. Guionneau, Crystallography and spin-crossover: a view of breathing materials, *Dalton Trans.* **43**, 382 (2014).
- [41] S. M. Neville, B. A. Leita, G. J. Halder, C. J. Kepert, B. Moubaraki, J.-F. Létard, and K. S. Murray, Understanding the two-step spin-transition phenomenon in iron(II) 1d chain materials, *Chem. Eur. J.* **14**, 10123 (2008).
- [42] D. Chernyshov, M. Hostettler, K. W. Törnroos, and H.-B. Bürgi, Ordering phenomena and phase transitions in a spin-crossover compound-uncovering the nature of the intermediate phase of [Fe(2-pic)₃]Cl₂ · ETOC, *Angew. Chem., Int. Ed.* **42**, 3825 (2003).
- [43] D. Paliwoda, L. Vendier, W. Nicolazzi, G. Molnár, and A. Bousseksou, Pressure tuning of coupled structural and spin state transitions in the molecular complex [Fe(H₂B(pz)₂(phen))], *Inorg. Chem.* **61**, 15991 (2022).
- [44] E. Collet, M. B.-L. Cointe, M. Lorenc, and H. Cailleau, State of the art and opportunities in probing photoinduced phase transitions in molecular materials by conventional and picosecond x-ray diffraction, *Z. Kristallogr. - Cryst. Mater.* **223**, 272 (2008).
- [45] M. Hostettler, K. Törnroos, D. Chernyshov, B. Vangdal, and H. Bürgi, Challenges in engineering spin crossover: Structures and magnetic properties of six alcohol solvates of Iron(II) Tris(2-picolylamine) dichloride, *Angew. Chem., Int. Ed.* **43**, 4589 (2004).
- [46] D. L. Reger, C. A. Little, V. G. Young, and M. Pink, Variable-temperature x-ray structural investigation of [Fe[HC(3,5-Me₂pz)₃]₂](BF₄)₂ (pz = Pyrazolyl Ring): observation of a thermally induced spin state change from all high spin to an equal high spin-low spin mixture, concomitant with the onset of nonmerohedral twinning, *Inorg. Chem.* **40**, 2870 (2001).
- [47] A. L. Thompson, A. E. Goeta, J. A. Real, A. Galet, and M. Carmen Muñoz, Thermal and light induced polymorphism in iron(II) spin crossover compounds, *Chem. Commun.* **2004**, 1390 (2004).
- [48] Z.-Y. Li, J.-W. Dai, Y. Shiota, K. Yoshizawa, S. Kanegawa, and O. Sato, Multi-step spin crossover accompanied by symmetry breaking in an Fe^{III} complex: Crystallographic evidence and DFT studies, *Chem. Eur. J.* **19**, 12948 (2013).
- [49] C.-J. Zhang, K.-T. Lian, S.-G. Wu, Y. Liu, G.-Z. Huang, Z.-P. Ni, and M.-L. Tong, The substituent guest effect on four-step spin-crossover behavior, *Inorg. Chem. Front.* **7**, 911 (2020).
- [50] C.-J. Zhang, K.-T. Lian, G.-Z. Huang, S. Bala, Z.-P. Ni, and M.-L. Tong, Hysteretic four-step spin-crossover in a 3d hofmann-type metal-organic framework with aromatic guest, *Chem. Commun.* **55**, 11033 (2019).
- [51] J. Zhang, W.-W. Yao, L. Sang, X.-W. Pan, X.-Z. Wang, W.-L. Liu, L. Wang, and X.-M. Ren, Multi-step structural phase transitions with novel symmetry breaking and inverse symmetry breaking characteristics in a [Ag₄I₆]²⁻ cluster hybrid crystal, *Chem. Commun.* **56**, 462 (2020).
- [52] M. Nishino, C. Enachescu, and S. Miyashita, Multistep spin-crossover transitions induced by the interplay between short- and long-range interactions with frustration on a triangular lattice, *Phys. Rev. B* **100**, 134414 (2019).
- [53] R. Traiche, M. Sy, and K. Boukheddaden, Elastic frustration in 1d spin-crossover chains: Evidence of multi-step transitions and self-organizations of the spin states, *J. Phys. Chem. C* **122**, 4083 (2018).

- [54] N. Sasaki and T. Kambara, Theory of the two-step spin conversion induced by the cooperative molecular distortions in spin-crossover compounds, *Phys. Rev. B* **40**, 2442 (1989).
- [55] A. Bousseksou, J. Nasser, J. Linares, K. Boukheddaden, and F. Varret, Ising-like model for the two-step spin-crossover, *J. Phys. I France* **2**, 1381 (1992).
- [56] A. Slimani, K. Boukheddaden, F. Varret, H. Oubouchou, M. Nishino, and S. Miyashita, Microscopic spin-distortion model for switchable molecular solids: Spatiotemporal study of the deformation field and local stress at the thermal spin transition, *Phys. Rev. B* **87**, 014111 (2013).
- [57] A. Slimani, K. Boukheddaden, and K. Yamashita, Effect of intermolecular interactions on the nucleation, growth, and propagation of like-spin domains in spin-crossover materials, *Phys. Rev. B* **92**, 014111 (2015).
- [58] J. A. Real, H. Bolvin, A. Bousseksou, A. Dworkin, O. Kahn, F. Varret, and J. Zarembowitch, Two-step spin crossover in the new dinuclear compound $[\text{Fe}(\text{bt})(\text{NCS})_2]2\text{bpym}$, with $\text{bt} = 2,2'$ -bi-2-thiazoline and $\text{bpym} = 2,2'$ -bipyrimidine: experimental investigation and theoretical approach, *J. Am. Chem. Soc.* **114**, 4650 (1992).
- [59] J. Cirera and E. Ruiz, Theoretical modeling of two-step spin-crossover transitions in Fe_{II} dinuclear systems, *J. Mater. Chem. C* **3**, 7954 (2015).
- [60] H. Romstedt, H. Spiering, and P. Gütllich, Modelling of two step high spin low spin transitions using the cluster variation method, *J. Phys. Chem. Solids* **59**, 1353 (1998).
- [61] Y. Singh, H. Oubouchou, M. Nishino, S. Miyashita, and K. Boukheddaden, Elastic-frustration-driven unusual magnetoelastic properties in a switchable core-shell spin-crossover nanostructure, *Phys. Rev. B* **101**, 054105 (2020).
- [62] M. Ndiaye and K. Boukheddaden, Pressure-induced multi-step and self-organized spin states in an electro-elastic model for spin-crossover solids, *Phys. Chem. Chem. Phys.* **24**, 12870 (2022).
- [63] R. Traiche, H. Oubouchou, and K. Boukheddaden, Elastic modeling of two-step transitions in sterically frustrated 1d binuclear spin-crossover chains, *Symmetry* **13**, 1836 (2021).
- [64] M. Ndiaye, N. E. I. Belmouri, J. Linares, and K. Boukheddaden, Elastic origin of the unsymmetrical thermal hysteresis in spin crossover materials: Evidence of symmetry breaking, *Symmetry* **13**, 828 (2021).
- [65] G. Azzolina, R. Bertoni, and E. Collet, General Landau theory of non-symmetry-breaking and symmetry-breaking spin transition materials, *J. Appl. Phys.* **129**, 085106 (2021).
- [66] M. Nishino, C. Enachescu, S. Miyashita, K. Boukheddaden, and F. Varret, Intrinsic effects of the boundary condition on switching processes in effective long-range interactions originating from local structural change, *Phys. Rev. B* **82**, 020409(R) (2010).
- [67] M. Ndiaye, Y. Singh, H. Fourati, M. Sy, B. Lo, and K. Boukheddaden, Isomorphism between the electro-elastic modeling of the spin transition and ising-like model with competing interactions: Elastic generation of self-organized spin states, *J. Appl. Phys.* **129**, 153901 (2021).
- [68] M. Ndiaye and K. Boukheddaden, Electro-elastic modelling of the two-step high-spin to low-spin relaxation with transient self-organized spin states in 2d spin crossover solids, *J. Phys. Soc. Jpn.* **89**, 014004 (2020).
- [69] S. B. Ogou, T. D. Oke, F. Hontinfinde, and K. Boukheddaden, Magnetic phase transitions in an electroelastic model for magnetically ordered spin-crossover solids, *Phys. Rev. B* **104**, 024431 (2021).
- [70] A. Slimani and K. Boukheddaden, Microscopic electroelastic modeling of a spin transition with symmetry breaking, *J. Appl. Phys.* **129**, 173901 (2021).
- [71] K. Boukheddaden, I. Shteto, B. Hôo, and F. Varret, Dynamical model for spin-crossover solids. I. Relaxation effects in the mean-field approach, *Phys. Rev. B* **62**, 14796 (2000).
- [72] W. Yu and P. Gielisse, High pressure polymorphism in cds, cdse and cdte, *Mater. Res. Bull.* **6**, 621 (1971).
- [73] J. Jung, F. Bruchhäuser, R. Feile, H. Spiering, and P. Gütllich, The cooperative spin transition in $[\text{Fe}_x\text{Zn}_{1-x}(\text{ptz})_6](\text{BF}_4)_2$: I. Elastic properties—an oriented sample rotation study by Brillouin spectroscopy, *Z. Phys. B* **100**, 517 (1996).
- [74] H. Spiering, K. Boukheddaden, J. Linares, and F. Varret, Total free energy of a spin-crossover molecular system, *Phys. Rev. B* **70**, 184106 (2004).
- [75] E. D. Loutete-Dangui, E. Codjovi, H. Tokoro, P. R. Dahoo, S.-i. Ohkoshi, and K. Boukheddaden, Spectroscopic ellipsometry investigations of the thermally induced first-order transition of $\text{RbMn}[\text{Fe}(\text{CN})_6]$, *Phys. Rev. B* **78**, 014303 (2008).
- [76] See Supplemental Material at <http://link.aps.org/supplemental/10.1103/PhysRevB.108.064107> for the spatiotemporal aspects and the comparison of the thermal hysteresis loops.
- [77] H. Oubouchou, A. Slimani, and K. Boukheddaden, Interplay between elastic interactions in a core-shell model for spin-crossover nanoparticles, *Phys. Rev. B* **87**, 104104 (2013).
- [78] J.-C. S. Levy, *Magnetic Structures of 2D and 3D Nanoparticles: Properties and Applications* (CRC Press, Boca Raton, FL, 2016).
- [79] A. Slimani, K. Boukheddaden, and K. Yamashita, Thermal spin transition of circularly shaped nanoparticles in a core-shell structure investigated with an electroelastic model, *Phys. Rev. B* **89**, 214109 (2014).
- [80] A. Slimani, K. Boukheddaden, F. Varret, M. Nishino, and S. Miyashita, Properties of the low-spin high-spin interface during the relaxation of spin-crossover materials, investigated through an electro-elastic model, *J. Chem. Phys.* **139**, 194706 (2013).
- [81] A. Slimani, H. Khemakhem, and K. Boukheddaden, Structural synergy in a core-shell spin crossover nanoparticle investigated by an electroelastic model, *Phys. Rev. B* **95**, 174104 (2017).
- [82] A. C. Felts, A. Slimani, J. M. Cain, M. J. Andrus, A. R. Ahir, K. A. Abboud, M. W. Meisel, K. Boukheddaden, and D. R. Talham, Control of the speed of a light-induced spin transition through mesoscale core-shell architecture, *J. Am. Chem. Soc.* **140**, 5814 (2018).
- [83] K. Affes, A. Slimani, Y. Singh, A. Maalej, and K. Boukheddaden, Magneto-elastic properties of a spin crossover membrane deposited on a deformable substrate, *J. Phys.: Condens. Matter* **32**, 255402 (2020).
- [84] K. Affes, H. Fourati, A. Slimani, and K. Boukheddaden, Effects of high-spin-low-spin lattice misfit on the nucleation and propagation velocities of elastic interfaces in cooperative spin-crossover solids, *J. Phys. Soc. Jpn.* **88**, 124701 (2019).
- [85] K. Affes, A. Slimani, A. Maalej, and K. Boukheddaden, Electro-elastic modeling of thermal and mechanical properties of a spin crossover core/shell nanoparticle, *Chem. Phys. Lett.* **718**, 46 (2019).